

A multivariate study of the rGO/g-C₃N₄ composite for the photocatalytic degradation of bisphenol A: Characterization, degradation kinetics, products identification, and ecotoxicity

Chubraider Xavier (✉ chubraiderxavier@usp.br)

Universidade de São Paulo <https://orcid.org/0000-0001-5858-1539>

Bianca Rebelo Lopes

UFSCar CCET: Universidade Federal de Sao Carlos Centro de Ciencias Exatas e de Tecnologia

Caue Ribeiro

Embrapa: Empresa Brasileira de Pesquisa Agropecuaria

Eduardo Bessa Azevedo

University of Sao Paulo Institute of Chemistry of Sao Carlos: Universidade de Sao Paulo Instituto de Quimica de Sao Carlos

Research Article

Keywords: rGO, g-C₃N₄, bisphenol A, heterogeneous photocatalysis, experimental design

Posted Date: June 18th, 2021

DOI: <https://doi.org/10.21203/rs.3.rs-415112/v1>

License:   This work is licensed under a Creative Commons Attribution 4.0 International License. [Read Full License](#)

Abstract

Bisphenol A (BPA), a common polymer plasticizer, is a contaminant of emerging concern with endocrine disrupting activity. Among existing abatement methods, photodegradation demands easily fabricated, inexpensive, high photoactive catalysts, leading to non-toxic byproducts after degradation. It is proposed an optimized (surface response methodology) catalyst for those goals: graphitic carbon nitride impregnated with reduced graphene oxide. The method was based on the sonication of preformed particles followed by reduction with hydrazine in reflux, a methodology that allows for better reproducibility and larger specific surface areas. The catalyst removed 90% of BPA (100 mL, 100 $\mu\text{g L}^{-1}$) in 90 min under UV irradiation (365 nm, 26 W) compared to 50% with pure g-C₃N₄ (pseudo-first-order kinetics). Tests with radicals scavengers revealed that superoxide radical was the main oxidation agent in the system. By mass spectrometry, two major degradation products were identified, which were less ecotoxic than BPA towards a series of organisms, according to *in silico* estimations performed with the ECOSAR 2.0 software.

1. Introduction

The use of water resources is a critical topic of discussion and technology development. 61% of the world population has no access to safely managed drinking water services, and approximately 48% of the population drinks water with no kind of treatment at all. Therefore, the importance of developing water treatment technologies is undeniable (UNESCO,2019).

The traditional drinking water treatment is mainly based on the physical-chemical processes of flocc-coagulation followed by decantation and disinfection. Those processes are not designed to remove pollutants that occur at concentrations ranging from ng L^{-1} to $\mu\text{g L}^{-1}$, which are not currently analyzed by the environmental agencies. Although those pollutants, known as Contaminant of Emerging Concern (CEC), may not cause acute effects on a variety of organisms, their chronic effects are reported in the literature (Ankley et al., 2008).

An example of CEC is bisphenol A (BPA), a plasticizer agent largely used in several industries, which presents endocrine disrupting activity. BPA-laden water consumption is associated with human health problems like infertility, obesity, cancer, and attention deficit hyperactivity disorder – ADHD (Ziv-Gal, Flaws, 2016; Wassenaar, et al., 2017; Rochester et al., 2018). Moreover, BPA is recalcitrant to chlorination and ozonation (Reddy et al., 2018).

Among the available methods for BPA abatement, heterogeneous photocatalysis is an efficient complementary technology to the traditional drinking water ones. That method is based on the light absorption capability of semiconductors, forming electron-hole pairs that perform redox reactions. The process efficiency is mainly affected by the charge carriers recombination time.

Titanium dioxide (TiO₂) is the most common semiconductor for that purpose due to relatively low recombination rates, but it only can be activated by ultraviolet light (UVA), rendering it less efficient for solar-based treatments (Moma, Baloyi, 2019). Several materials (ZnO, Mn_xO_y, CdS), with smaller bandgaps, have been reported as replacements for TiO₂, as they may be more easily activated by solar light. However, metal-based semiconductors may ultimately contaminate the treated water with metallic ions (secondary pollution), motivating research about metal-free semiconductors (Cao et al., 2013; Obregón, Colón, 2014; Adhikari et al, 2015; Ai et al., 2015).

Graphitic carbon nitride (g-C₃N₄) is an adequate choice due its simple preparation from inexpensive precursors (melamine or urea) and high synthesis throughput. Although it is activated by visible light, its charge recombination rate is high (Ai et al., 2015; Chen et al., 2016). To increase its charge separation, g-C₃N₄ can be associated with reduced graphene oxide (rGO), producing a metal-free composite, where rGO concentrates electrons, while g-C₃N₄ is expected to concentrate holes [Hao et al., 2017; Gu et al., 2018; Qian et al. 2018, Wan et al., 2018).

rGO is produced by the reduction of graphene oxide (GO), from graphite oxide (GrO) exfoliation – an inexpensive precursor as well. It is largely associated with a variety of semiconductors, enhancing their photocatalytic activity by acting as an electron-acceptor (Mural et al., 2015; Nikokavoura, Trapalis, 2017; 2018; Meng, Zhang, 2018).

rGO/g-C₃N₄ composites can be produced by thermal or sonochemical approaches (Wan et al., 2018, Aleksandrak, et al., 2017). While the thermal path usually leads to poor distribution of rGO into the g-C₃N₄ matrix, the sonochemical approach may generate materials with larger specific surface areas, materials with improved reduction, besides less energy consumption in comparison to the other path. Moreover, the experimental conditions are easily controlled and reproduced (Duan et al., 2015).

Although rGO/g-C₃N₄ preparation conditions have been previously described, the photocatalytic efficiencies of the prepared composites were very different, even in similar works that typically report the photocatalytic degradation of synthetic dyes or phenol halides (Ai et al., 2015; Gu et al., 2018; Aleksandrak et al., 2017). It lacks information about the efficiency of rGO/g-C₃N₄ for degrading CECs like BPA. Moreover, all those papers used a univariate approach for improving the degradation outcome, possibly leading to pseudo-optimal conditions, and not actually the best ones (Bruns et al., 2006). Therefore, the objective of the present work was to perform a multivariate optimization of the rGO/g-C₃N₄ composite synthesis aiming at increasing its photocatalytic activity, employing the response surface methodology and using BPA photodegradation as the response-variable. The composite was characterized and the BPA degradation kinetics and mechanism were studied. Furthermore, photodegradation products were determined and their respective ecotoxicities estimated.

2. Experimental Section

2.1 Materials

Melamine (99%, Sigma-Aldrich), graphite powder (99%, Synth LDT), potassium permanganate (99%, Synth LDT), and hydrogen peroxide (30%, Synth LDT), sulfuric acid (96%, AppliChem Panreac), hydrochloric acid (37%, Chemis) and aqueous hydrazine (80%, Merck) were used as received.

2.2 Synthesis of the g-C₃N₄

Graphitic carbon nitride (g-C₃N₄) was synthesized by the methodology developed from previous works (Cadan et al., 2021). Two milligrams of melamine were put into a porcelain crucible (model A-45 with cover) and pyrolyzed in a muffle furnace (EDG 7000 coupled to an EDG heater EDGCON 3P).

Melamine was heated, from room temperature to 50°C, at a rate of 10°C min⁻¹ and held at that temperature for 30 min. Then the powder was heated from 50 to 605°C at a rate of 6°C min⁻¹. The system remained at that temperature for 183 min. Then, the material was naturally cooled to room temperature.

The collected material was ground in an agate mortar/pestle and transferred to Falcon® tubes (50 mL) which were kept away from light. The amount of g-C₃N₄ needed for performing all experiments were produced and homogenized.

2.3 Synthesis of GrO

Graphite oxide, GrO, was synthesized by a modified Hummers methodology adapted from Chen et al. (2013) – more details are given in the Supplementary Material. Graphite powder (1.00 g) was mixed with 70 mL of concentrated sulfuric acid in a 2-L beaker. To this mixture, 9.00 g of potassium permanganate were added. The system was heated to 40 °C and magnetically stirred for 40 min. Then, 150 mL of ultrapure water was poured into it. Finally, 500 mL of ultrapure

water were added to the flask. It was magnetically stirred for 15 min more and 10.0 mL of concentrated hydrogen peroxide (10 mol L^{-1}) were slowly added.

This mixture was magnetically stirred for 20 min and vacuum filtered. The material was suspended in 250 mL of hydrochloric acid 1.0 mol L^{-1} and vacuum filtered again. The amount of synthesized GrO required for all experiments was prepared and homogenized. The solid was previously frozen, grounded, and dialyzed with a membrane capable of removing ions from 8,000 to 14,000 Da. The external solution was renovated every 2 h during the first day, every 4 h during the second one, and then every 12 h thereafter, until the spent water pH matched the one of ultrapure water (pH meter Marconi PA 200). The purified material was air-dried and lyophilized for six days. This material was ground into an agate mortar/pestle and transferred to Falcon® tubes (50 mL) which were also kept away from light.

2.4 Preparation of the rGO/g-C₃N₄

The composite was prepared by a sonochemical route. Required amounts of g-C₃N₄ and GrO were weighed to prepare 1.0 g L^{-1} suspensions. Those suspensions were sonicated in parallel with the aid of two ultrasound (tip) devices (BRANSON model 450 and 550, for GO and g-C₃N₄, respectively) with power of 14 W (3 s on, 7 s off) for 1.5 h. The suspensions were then mixed and magnetically stirred and the pH was adjusted to 3.0 by the addition of H₂SO₄ 3.0 mol L^{-1} . After 20 min, the mixture was sonicated again by the same routine for a specific time. To the sonicated mixture, a certain amount of hydrazine was added. That mixture was refluxed at 98 °C for 24 h. That suspension was naturally cooled down to room temperature and vacuum filtered through 0.45 µm pore diameter cellulose acetate membranes. The composite was air-dried during 24 h, away from light, grounded using an agate mortar/pestle, and stored in 1.5-mL Eppendorf® tubes.

2.5 Optimization of the rGO/g-C₃N₄ synthesis

The response surface methodology (RSM) was used for optimizing the composite synthesis (Bruns et al., 2006). The response-variable was BPA degradation. For more details, please check the Supplementary Material.

Initially, a 2³ full factorial design (in duplicate) was performed. Three factors were studied: weight percentage of GrO in the mixture prior to reduction (%GrO), the mixture sonication time, and the N₂H₄:GrO weight ratio.

Second, based on the obtained results, a polynomial was adjusted to the data and a set of experiments (according to Equation SM4) were performed along the path of steepest ascent, i.e., towards increasing BPA degradation.

Finally, over the region with the greatest BPA degradations, a central composite design (CCD) was performed. Another polynomial was adjusted to the data. The maximum of that polynomial estimates the best synthetic conditions that would maximize BPA degradation. An analysis of variance (ANOVA) was performed to check the fitting of the model generated.

2.6 Characterizations

For the precursors and the optimized composite, X-ray diffraction (XRD), Fourier transform infrared spectrophotometry (FTIR), N₂ physisorption using the Brunauer-Emmett-Teller (BET) isotherm, dynamic light scattering – zeta potentials (ZP), scanning electron microscopy with field emission gun (SEM-FEG), energy dispersive spectroscopy (EDS), diffuse reflectance spectroscopy (DRS) with the Tauc plot approach (Khan et al., 2017), and elemental analysis (CHNS) were performed, as described in the Supplementary Material.

2.7 Photodegradation experiments

Photodegradation experiments were performed in a 250-mL, temperature-controlled open-jacketed reactor maintained at 20°C. Typically, 100 mL of BPA $100 \mu\text{g L}^{-1}$ at pH 6.0 (adjusted with aqueous ammonia) and 5.0 mg of catalyst (composite) were put into the reactor and kept under magnetic stirring and air bubbling (approximately 270 mL min^{-1}) in the dark for 30 min. Then, a black light blue (BLB) lamp (Empalux®, 25 W) placed 15 cm over the suspension surface was turned on for 60 min. Afterwards, the irradiated suspension was filtered through 0.45 μm pore diameter cellulose acetate membranes, stored in amber flasks, and kept in the fridge (5°C) until the extraction step. Adsorption and photolysis experiments were performed in the same manner, except for the absence of light and catalyst, respectively.

2.8 Extraction step and HPLC analyses

Extraction was performed by the vortex-assisted liquid-liquid microextraction (VALLME) technique, based on Yantzi et al. (2010). To a glass tube, containing 10.0 mL of sample, 100 μL of *n*-octanol were added without spraying it into the bulk of the sample. The tube was vortex-stirred at 3,800 rpm for 2.5 min and centrifuged with a relative centrifugal force (RCF) of 1,264 g at 25°C for 20 min. The organic phase was collected with a liquid chromatographic syringe (25 μL , Hamilton series 700 with fused needle), placed in a 100- μL insert inside an 1.5-mL amber chromatographic vial.

HPLC analyses were performed in a Shimadzu chromatograph equipped with a LC-20AT single pump, manual injection by a six-port valve (20 μL of loop injection), CBM-20A controller powered by LCsolutions® software, DGU-20A₅ degasser, and SPD-20A UV-vis detector. A Luna® 5 μm C8(2) 100 Å, 150 × 4.6 mm, LC column was used. Mobile phase was 1:1 acetonitrile and water with 1% acetic acid. Chromatographic conditions were: injection volume 20 μL , reversed mode of elution, isocratic mode, flow 1.00 mL min^{-1} , detection at 230 nm, total run time 8 min, and BPA retention time 5.3 min.

2.9 Kinetic and scavenging experiments

Degradation kinetics experiments (optimized composite) were performed as described in item 2.7, except for using 10.0 mg of the catalyst instead of 5.0 mg. All experiments were randomly performed in triplicate. Experiments with scavengers (2.0 mmol L^{-1} each) were also performed as described by Wang et al. (2019), for irradiation periods of 60 min. The scavengers were added just before the BLB lamp was turned on (Table 1).

Table 1
– Scavengers and respective inhibited species

Scavenger	Inhibited species
propan-2-ol (IPA)	hydroxyl radical ($\bullet\text{OH}$)
benzoquin-1,4-one (BQ)	superoxide radical ($\text{O}_2^{\bullet-}$)
potassium iodide (KI)	holes in the valence band (h_{BV}^+)

2.10 Identification of the degradation products and ecotoxicity estimative

The experiments were performed in a Shimadzu LC-MS/MS equipment: LC-20AD Prominence Series UFLC pumps coupled to a Bruker Daltonics Esquire 6000 Ion Trap (IT) equipped with an electrospray ion source (ESI) source. The analyses conditions were: column x-TERRA MS (WATERS™) 5.0 μm 150 · 2.1 mm, gradient elution with 0.05% ammonium hydroxide in water (A) and 0.05% ammonium hydroxide in acetonitrile (B) from 20% (B) to 90% (B) in 10 min, hold for 2 min, then to 20% in 15 min, flow rate $0.250 \text{ mL min}^{-1}$, injection volume 15 μL . The mass spectrometer conditions were: negative ionization mode, scan mode in the range of 50 – 500 Da, dry gas flow rate 8.0 L min^{-1} , nebulizer 20 psi, dry temperature 300°C, capillary voltage 3,500 V. Ecotoxicities were estimated using the freeware Ecological Structure-Activity Relationships (ECOSAR) 2.0.

3. Results And Discussion

3.1 Pre-optimization experiments (Zeta potential determination)

Zeta potential (ZP) was measured at different pH values in order to determine the pH in which the precursors had opposite charges, since the critical steps of the composite formation is the electrostatic agglomeration of pre-formed particles. At pH 3.0, the surface charge of g-C₃N₄ and the exfoliated GrO (called graphene oxide, GO) are approximately +7.96 and -32.7 mV, respectively, as shown in Figure SM1. That pH value was used in all syntheses.

3.2 Optimization of the formation of rGO/g-C₃N₄

Initially, a 2³ (3 factors, 2 levels) full factorial design in duplicate was performed, generating 16 experiments, as shown in Table SM1. The estimated experimental error was 1.9% (Equation SM2). That error was low as it encompasses several steps (catalyst synthesis, photocatalytic experiments, extraction, and HPLC analyses).

A first-order polynomial model (Equation 1) was adjusted to the results of these first experimental design, in which x_1 , x_2 , and x_3 are: weight percentage of GrO in the mixture prior to reduction (%GrO), the mixture sonication time, and the N₂H₄:GrO weight ratio, respectively, in coded factors (Equation SM1).

$$\text{Removal (\%)} = 23.5 + 5.25x_1 - 2.45x_2 + 5.20x_1x_2 + 6.32x_1x_3 \quad (1)$$

$\pm 0.465 \quad \pm 0.930 \quad \pm 0.930 \quad \pm 0.930 \quad \pm 0.930$

Main and interaction effects, along with their statistical significance (95% confidence interval), are presented in Figure SM2. It is possible to observe that the GrO amount and the sonication time were statistically significant, as well as the interaction between them. Increasing GrO amount causes an increment in the answer just as decreasing sonication time does. This might happen because increasing the GrO amount means increasing the number of electrons acceptors in the material, what makes it possible extended charge separation; meanwhile, decreasing sonication time also decreases the exfoliation of the formed composite, what would cause g-C₃N₄ to separate itself from rGO (instead of a true composite, one would simply get a physical mixture). Although the interaction between GrO amount and GrO:N₂H₄ weight ratio was statistically significant, the GrO:N₂H₄ weight ratio factor itself was not statistically significant within the studied levels. This might mean that, in both levels, hydrazine was in excess. Thus, the amount of hydrazine was set at its lower level in the following experiments.

The experimental conditions with which the best BPA removal was achieved, along the path of steepest ascent (Table SM2), were used as the central point of a CCD (Table SM3). The model proposed for de CCD is shown in Eq. (2).

$$\text{Removal (\%)} = 61.0 - 8.65x_1 - 2.52x_2 + 4.73x_1x_2 - 8.98x_1^2 - 7.83x_2^2 + 5.78x_1^3 \quad (2)$$

$\pm 0.917 \quad \pm 1.78 \quad \pm 0.562 \quad \pm 0.794 \quad \pm 0.669 \quad \pm 0.669 \quad \pm 1.12$

Equation 2 generates the surface in Figure SM3. The model was well adjusted according to an ANOVA (Table SM4) and the Fisher's statistics. The respective maximum (optimum synthetic conditions) could be estimated: $x_1 = -0.039$ and $x_2 = -0.26$, i.e., %GrO = 15% and sonication time = 7 min e 20 s, respectively. One can observe the improvement achieved regarding BPA removal, which varied from 24% (central point conditions, initial 2^3 full factorial design) to 65% (optimal conditions, CCD) — a three-fold increase, approximately. All of the following results were obtained with the optimized material.

3.3 Characterization

According to the XRD analysis (Fig. 1) both precursor materials were formed and the composite crystalline structure did not differ from the one of g-C₃N₄, agreeing with Gu et al. (2018) and Liu et al. (2016). That can be attributed to: (a) rGO produces low-intensity signals in XRD; and (b) low rGO content in the composite, small enough not to change the g-C₃N₄ crystalline structure.

GrO is characterized by the single peak at 11.6° related to (1 0 0), matching JCPDS file 75-2078, in accordance with the literature (Aleksandrak et al., 2017; Blanton and Majumdar, 2013; Chen et al., 2017; He et al., 2018). g-C₃N₄ presents two major peaks at 13.2° (1 0 0) and 26.6° (0 0 2), and minor peaks at 44.6° (2 0 0) and 56.4° (0 0 4), matching JCPDS file 87-1526. Those results were also reported by Cao et al. (2013), Ma et al. (2014), and Sun et al. (2017).

The microstructures (Fig. 2) suggest that precursors and composite particles have no particular habit, within a micrometric scale. The materials in the composite are undistinguishable, being clusters of precursor layers. The observed lamellar clustering (Figs. 5c) could be associated with the synthesis based on the self-assembling of bidimensional precursors. g-C₃N₄ and GrO specific surface areas (SA) were approximately 25.8 and 160 m² g⁻¹, respectively. The SA of the optimized material was 85.9 m² g⁻¹, while g-C₃N₄ under identical exfoliation conditions (no GrO) was 31.7 m² g⁻¹, indicating that rGO alters the specific surface area of the composite, probably by unpacking g-C₃N₄ layers due an electrostatic effect. As a matter of fact, the expected SA for the simple mixture of g-C₃N₄ and rGO in the same content (16% rGO) is 47 m².g⁻¹, confirming the SA increasing effect.

The pH of the composite formation (set in 3.0) also can be associated to the SA since pH affects how well the exfoliation and agglomeration of the material occur (Silva et al., 2017). The ZP curve (Figure SM4) of the composite shows that the optimized material follows the same profile of pristine g-C₃N₄, previously shown (Figure SM1).

By the EDS results (Figure SM5), one can observe that pure g-C₃N₄ was formed, considering that the employed solid-phase synthesis required only one reagent. The small content of impurities (1.92%) is derived from the sample holder. Apparently, the contact with atmospheric air during pyrolysis allowed a partial oxidation during the annealing. That would explain the presence of oxygen in the EDS analyses.

GrO (Figure SM6) was still impregnated with a small amount of sulfur, chlorine, and manganese, even after the exhaustive purification. Nevertheless, as that residual contamination is small (2.21%), the material was considered suited for the next synthetic steps. Again, 1.19% of impurities came from the sample holder. Finally, looking at the optimized material (Fig. 3), it did not show impurities, except for 3.25% from the sample holder.

Aiming at estimating the rGO content in the synthesized photocatalyst, CHNSO analyses were performed. First, the g-C₃N₄ precursor was analyzed and the nitrogen content was determined. Second, the composite was also analyzed and,

using that previous nitrogen content, the amount of g-C₃N₄ was calculated. By subtracting the g-C₃N₄ mass from the composite one, the rGO mass was calculated. Therefore, the rGO content in the composite was estimated as approximately 4.0%.

Precursors and the optimized material were also characterized by their FTIR spectra (Fig. 4, Table 2). Bands were identified in accordance with the work of Aleksandrak et al. (2017). Reduced graphene oxide was almost free from oxygen and it was mainly composed of carbon and hydrogen (small electronegativity difference). Therefore, the spectrum of the optimized material is similar to the one of g-C₃N₄, as the magnet dipoles of the chemical bonds are not high enough for coupling with the infrared waves emitted by the source.

Table 2 - Attribution of the bands from the FTIR analysis

Band	Wave number (cm ⁻¹)	Attribution
I (a)	1057	stretching vibration of C-O bonds of alkoxy groups
II (a)	1620	stretching and bending vibration of OH groups
III (a)	1726	stretching vibration of C=O of carboxyl groups
IV (a)	3320	Stretching of the O-H bonds in hydroxyl groups
I (b)	806	breathing mode of the triazine units
II (b)	1234;1313; 1398	stretching modes of C-N bond in heterocycles
III (b)	1625	stretching mode of C=N bonds
IV (b)	3130	stretching modes of secondary and primary amines

Reduced graphene oxide changes from bright yellow g-C₃N₄ to a dark gray material, which explains the lower reflectance of the composite (Fig. 5a). In the DRS analysis, one can observe that the band gap of g-C₃N₄ did not change significantly by the presence of rGO in the structure (Fig. 5b).

rGO is a conductor species (no significant charge separation) with a transition considered to be direct and allowed ($r = 0.5$). Therefore, oxidation reactions are promoted by g-C₃N₄, suggesting that the improved photocatalytic activity of the material may be due to increased specific surface areas and low recombination rates – charge transfer to rGO (Malagutti et al., 2009).

VB (+1.55 eV) and CB (-1.09 eV) potentials for g-C₃N₄ were estimated by the empiric Equations SM6-8 (Mousavi et al., 2016). As rGO exhibits no significant charge separation (Fig. 5a) and pure g-C₃N₄ and the composite band gaps were almost the same (Fig. 5b), the estimated band positions for g-C₃N₄ were considered to be the same for the composite. 3.4 Degradation kinetics and scavenging tests

Figure 6 presents the BPA degradation kinetics. Both pure g-C₃N₄ and optimized rGO/g-C₃N₄ followed a pseudo-first order behavior, with $k' = (0.94 \pm 0.019) \cdot 10^{-2} \text{ min}^{-1}$ ($R^2 = 0.981$) and $k'' = (2.0 \pm 0.083) \cdot 10^{-2} \text{ min}^{-1}$ ($R^2 = 0.986$), respectively. Therefore, rGO/g-C₃N₄ removed BPA approximately 2.4 times faster than g-C₃N₄ alone. Dark adsorption and direct photolysis after 90 min, 10.7 and 6.2%, respectively, also shown in Fig. 3, were much less significant than heterogeneous photocatalysis.

Scavenging tests (Table 3) pointed out that the main species involved in BPA degradation was the superoxide radical (Ji et al., 2013; Wang et al., 2017). It was also possible to observe that holes and hydroxyl radicals were not really important for the degradation of the target molecule. Taking into account the scavenging tests results, the calculated VB and CB potentials, and the necessary potentials for generating O₂^{•-} and •OH (all of them against the NHE), it becomes clear that aqueous O₂^{•-} could be easily formed in the presence of the composite, once its CB potential was -1.09 eV and the reduction potential of O₂ into O₂^{•-} is -0.33 eV (Malagutti et al., 2009), approximately 3 times lower (in absolute values). On the other hand, it is straightforward why •OH did not play any significant role in the degradation process. The

oxidation potential of H₂O into •OH is + 2.80 eV (Bauer and Fallmann, 1997), approximately 2 times higher than the VB potential (+ 1.55 eV). However, the material is able to oxidize H₂O into O₂, as the VB potential is greater than + 1.23 eV (Zhao et al., 2014). In summary, the BPA degradation mechanism was based on the superoxide radical chemistry, formed when the composite CB reduces dissolved molecular oxygen.

Table 3 - BPA degradations with scavengers

Scavenger	Removal (%)
None	65.0
IPA	64.5
BQ	42.0
KI	60.0

IPA = propan-2-ol; BQ = benzoquin-1,4-one; KI = potassium iodide

3.5 Degradation Products Identification and Ecotoxicity

Two major degradation products (DPs) were identified: 4-(2-(3,4-dihydroxyphenyl)propan-2-yl)cyclohexa-3,5-diene-1,2-dione (DP1) and 4,4'-(propane-2,2-diyl)bis(cyclohexa-3,5-diene-1,2-dione) (DP2). Their structures are shown in Fig. 7 and their mass spectra are given in Figure SM7. Those molecules were also detected by Kondrakov et al. (2014).

Two concurrent degradation mechanisms were proposed in Fig. 8, as the major oxidizing agent acting in the treatment was the superoxide radical. In path (1), superoxide radical abstracts a proton from BPA (-OH moiety) forming a hydroperoxyl radical. The deprotonated oxygen atom can form a double bond, allowing the hydroperoxyl radical to attack the carbon vicinal to the formed ketone. The added hydroperoxyl radical removes a proton from that carbon, triggering the elimination of water and forming a double bond with the remaining oxygen atom.

In path (2), superoxide radical adds a radicalar oxygen to BPA (vicinal carbon to the -OH moiety) and a hydroxyl ion is eliminated. The radicalar oxygen can abstract a proton from water forming hydroxyl radical in the process. Therefore, DP1 is formed when BPA reacts by paths (1) and (2); DP2 when BPA reacts only by path (1) or when DP1 undergoes oxidation (Li, Kuo, Weeks Junior, 1979; Lerner et al., 2006).

Figure 9 shows the estimated ecotoxicities of BPA and the proposed DPs by the ECOSAR 2.0 software. LC₅₀ and EC₅₀ are the concentrations in which a single exposition to a chemical species, during a specific period of time, promotes death or deleterious effects to 50% of a tested population. On the other hand, ChV is the chronic value, i.e., the concentration in which a continuous exposition promotes chronic effects (Gupta, 2018). According to the Globally Harmonized System of Classification and Labeling of Chemicals (GHS), the ratio (R) between the acute effect (LC₅₀ or EC₅₀) and

the chronic one (ChV) determines the ecotoxicity of a compound: Very toxic (R ≤ 1),

Toxic (1 < R ≤ 10), Harmful (10 < R ≤ 100), and Not harmful (R > 100) (The United Nations, 2017).

As expected, BPA was very toxic or toxic to all of the test-organisms, both for acute and chronic exposures. One can see that DP2 was less toxic for all the organisms for both levels of exposure, being even not harmful for fishes within acute level. DP1 was also less harmful than BPA for all the organisms in both levels. Therefore, the proposed treatment is effective for BPA removal because it not just can degrade the BPA molecule but also convert it to less toxic species.

4. Conclusions

- The multivariate approach was helpful for determining the conditions in which materials with optimized photocatalytic properties could be synthesized.

- The use of the sonochemical approach was useful for keeping the experimental conditions reproducible, what is reflected by the low experimental error of the experimental design. It was also helpful for obtaining a material with large specific surface area.
- The use of bisphenol A as model-pollutant at environmental concentrations helped in getting closer-to-real-life treatment conditions, although that makes analytical procedures more challenging.
- Characterizing this kind of composite, in which precursors have similar structures and compositions, is a true challenge because it is hard to notice any differences in a variety of techniques (FTIR, XRD, SEM, etc.).
- Although the analytical signals of rGO were hard to perceive, its presence in the composite could be inferred by the increased specific surface area and the photocatalytic activity of the composite.
- The photocatalytic BPA degradation exhibited a pseudo-first-order kinetics, both for g-C₃N₄ and the composite. The degradation rate, using the synthesized composite as the photocatalyst, was twice as fast as the one with g-C₃N₄.
- The main oxidizing species generated by the composite was O₂^{•-}, according to the calculated band positions and scavenging tests.
- The synthesized material was able to successfully degrade and partially detoxify BPA in a relatively short period of time.

Declarations

ETHICAL Approval

No ethics approval was necessary for this work.

Consent to participate

All authors gave their consent to participate.

Consent to publish

All authors gave their consent to this publication.

Authors contributions

All authors have contributed to this work. Chubraider Xavier wrote the paper and performed the majority of the experiments. Bianca Rebelo Lopes performed the mass spectrometry experiments and wrote the respective part of the Material and Methods section; Caue Ribeiro discussed the ideas with the authors and reviewed the paper; Eduardo Bessa Azevedo discussed the ideas, supervised the work, and reviewed the paper.

Funding

The authors would like to thank The National Council for Scientific and Technological Development (CNPq), grant # 140410/2019-8, The Coordination for the Improvement of Higher Education Personnel (CAPES – Finance Code 001), São Paulo Research Foundation (FAPESP), process # 2018/01258-5 and The Research Network of Nanotechnology Applied to Agribusiness (AgroNano Network/Embrapa, MCTI-SisNano) for financial support.

Competing interests

There is no conflict or competing interests for this work.

Availability of data and materials

All data and supplementary materials are available for consult.

ACKNOWLEDGEMENTS

The authors also thank Professor Quezia Bezerra Cass for making the mass spectrometry analyses possible.

References

1. Adhikari SP, Pant HR, Kim HJ, Park CH, Kim CS (2015) Deposition of ZnO flowers on the surface of g-C₃N₄ sheets via hydrothermal process. *Ceram Int* 41(10):12923–12929. DOI:10.1016/j.ceramint.2015.06.134
2. Ai B, Duan X, Sun H, Qiu X, Wang S Metal-free graphene-carbon nitride hybrids for photodegradation of organic pollutants in water. *Catal. Today*, 258 (2015) Part 2, 668–675. DOI: 10.1016/j.cattod.2015.01.024
3. Aleksandrak M, Kukulka W, Mijowska E (2017) Graphitic carbon nitride/graphene oxide/reduced graphene oxide nanocomposites for photoluminescence and photocatalysis. *Appl Surf Sci* 398:56–62. DOI:10.1016/j.apsusc.2016.12.023
4. Ankley GT, Erickson RJ, Hoff DJ, Mount DR, Lazorchak J, Beaman J, Linton TK (2008) Aquatic life criteria for contaminants of emerging concern: Part I General challenges and recommendations. USA, EPA. https://www.epa.gov/sites/production/files/2015-08/documents/white_paper_aquatic_life_criteria_for_contaminants_of_emerging_concern_part_i_general_challenges_and_recommendations1.pdf (Accessed 02 August 2020)
5. Bauer R, Fallmann H (1997) The photo-Fenton oxidation – A cheap and efficient wastewater treatment method. *Res Chem Intermediat* 23(4):341–354. DOI:10.1163/156856797X00565
6. Blanton TN, Majumdar D (2013) Characterization of X-ray irradiated graphene oxide coatings using X-ray diffraction, X-ray photoelectron spectroscopy, and atomic force microscopy. *Powder Diffr* 28 2:68–71. DOI:10.1017/S0885715613000109
7. Bruns RE, Scaramino IS, Barros Neto B *Statistical Design – Chemometrics*. First edition, Elsevier: Amsterdam, 422 p., 2006. ISBN-13: 978-0444521811\$4
8. Cadan FM, Ribeiro C, Azevedo EB (2021) Improving g-C₃N₄: WO₃ Z-scheme photocatalytic performance under visible light by multivariate optimization of g-C₃N₄ synthesis. *Appl Surf Sci* 537:147904–114917. DOI:10.1016/j.apsusc.2020.147904
9. Cao S-W, Yuan Y-P, Fang J, Shahjamali MM, Boey FY, Barber J, Loo SCJ, Xue C (2013) In-situ growth of CdS quantum dots on g-C₃N₄ nanosheets for highly efficient photocatalytic hydrogen generation under visible light irradiation. *Int J Hydrogen Energ* 38(3):1258–1266. DOI:10.1016/j.ijhydene.2012.10.116
10. Chen J, Yao B, Li C, Shi G (2013) An improved Hummers method for eco-friendly synthesis of graphene oxide. *Carbon* 64:225–229. DOI:10.1016/j.carbon.2013.07.055
11. Chen K, Chai Z, Li C, Shi L, Liu M, Xie Q, Zhang Y, Xu D, Manivannan A, Liu Z (2016) Catalyst-free growth of three-dimensional graphene flakes and graphene/g-C₃N₄ composite for hydrocarbon oxidation. *ACS Nano* 10(3):3665–3673. DOI:10.1021/acsnano.6b00113
12. Chen Q, Cai D, Zhan H (2017) Construction of reduced graphene oxide nanofibers and cobalt sulfide nanocomposite for pseudocapacitors with enhanced performance. *J Alloy Compd* 706:126–132. DOI:10.1016/j.jallcom.2017.02.189
13. Duan H, Wang D, Li Y (2015) Green chemistry for nanoparticle synthesis. *Chem Soc Rev* 44:16, 5778–5792. DOI:10.1039/C4CS00363B
14. Gu Y, Yu Y, Zou J, Shen T, Xu Q, Yue X, Meng J, Wang J (2018) The ultra-rapid synthesis of rGO/g-C₃N₄ composite via microwave heating with enhanced photo-catalytic performance. *Mater Lett* 232:107–109.

15. Gupta PK (Ed.) General toxicology. In: Illustrated Toxicology: With study questions. 1. Ed. Academic Press: London, UK, 2018,1–65. ISBN 978-0-12-813213-5
16. Hao Q, Hao S, Niu X, Li X, Chen D, Ding H (2017) Enhanced photochemical oxidation ability of carbon nitride by π - π stacking interactions with graphene. *Chinese J Catal* 38(2):278–286. DOI:10.1016/S1872-2067(16)62561-5
17. He H, Huang L, Zhong Z, Tan S (2018) Constructing three-dimensional porous graphene-carbon quantum dots/g-C₃N₄ nanosheet aerogel metal-free photocatalyst with enhanced photocatalytic activity. *Appl Surf Sci* 441:31, 285–294. DOI:10.1016/j.apsusc.2018.01.298
18. Ji H, Chang F, Hu X, Qin W, Shen J (2013) Photocatalytic degradation of 2,4,6-trichlorophenol over g-C₃N₄ under visible light irradiation. *Chem Eng J* 218:183–190. DOI:10.1016/j.cej.2012.12.033
19. Khan H, Rigamonti MG, Patience GS, Boffito DC (2017) Spray dried TiO₂/WO₃ heterostructure for photocatalytic applications with residual activity in the dark. *Appl Catal B-Environ* 226:311–323. DOI:10.1016/j.apcatb.2017.12.049
20. Kondrakov AO, Ignatev AN, Frimmel FH, Bräse S, Horn H, Revelsky AI. Formation of genotoxic quinones during bisphenol A degradation by TiO₂ photocatalysis and UV photolysis: A comparative study. *Appl. Catal. B-Environ.*, 160–161 (2014), 106–114. DOI: 10.1016/j.apcatb.2014.05.007
21. Lerner H-W, Margraf G, Kretz T, Schiemann O, Bats J, Dürner G, Fabrizi de Biani, F, Zanella P, Bolte M, Wagner M (2006) Redox behaviour of pyrazolyl-substituted 1,4-dihydroxyarenes: Formation of the corresponding semiquinones, quinhydrones and quinones. *Z Naturforsch B* 61:252–264. DOI:10.1515/znb-2006-0304
22. Li KY, Kuo CH, Weeks Junior JL (1979) A kinetic study of ozone-phenol reaction in aqueous solutions. *AIChE J* 25(4):583–591. DOI:10.1002/aic.690250403
23. Liu Q, Guo Y, Chen Z, Zhang Z, Fang X (2016) Constructing a novel ternary Fe(III)/graphene/g-C₃N₄ composite photocatalyst with enhanced visible-light driven photocatalytic activity via interfacial charge transfer effect. *Appl Catal B-Environ* 183:231–241. DOI:10.1016/j.apcatb.2015.10.054
24. Ma TY, Tang Y, Dai S, Qiao SZ (2014) Proton-functionalized two-dimensional graphitic carbon nitride nanosheet: An excellent metal-/label-free biosensing platform. *Small* 10:12, 2382–2389. DOI:10.1002/smll.201303827
25. Malagutti AR, Mourão HAJL, Garbin JR, Ribeiro C (2009) Deposition of TiO₂ and Ag:TiO₂ thin films by the polymeric precursor method and their application in the photodegradation of textile dyes. *Appl Catal B-Environ* 90:205–212. DOI:10.1590/1980-5373-MR-2015-0358
26. Meng X, Zhang Z (2018) Two dimensional graphitic materials for photoelectrocatalysis: A short review. *Cat Today* 315:2–8. DOI:10.1016/j.cattod.2018.03.015
27. Moma J, Baloyi J Modified titanium dioxide for photocatalytic applications. In: KHAN, S. B.; AKHTAR, K (Org.) *Photocatalysts: Applications and attributes*. First Edition, IntechOpen Limited: London, 156 p., 2019. ISBN: 978-1-78985-476-3
28. Mousavi M, Habibi-Yangjeh A, Abitorabi M (2016) Fabrication of novel magnetically separable nanocomposites using graphitic carbon nitride, silver phosphate and silver chloride and their applications in photocatalytic removal of different pollutants using visible-light irradiation. *J Colloid Interf Sci* 480:218–231. DOI:10.1016/j.jcis.2016.07.021
29. Mural PKS, Sharma M, Madras G, Bose S (2015) A critical review on in situ reduction of graphene oxide during preparation of conducting polymeric nanocomposites. *RSC Advances* 5:41, 32078–32087. DOI:10.1039/C5RA02877A
30. Nikokavoura A, Trapalis C (2017) Alternative photocatalysts to TiO₂ for the photocatalytic reduction of CO₂. *Appl Surf Sci* 391:149–174. DOI:10.1016/j.apsusc.2016.06.172
31. Nikokavoura A, Trapalis C (2018) Graphene and g-C₃N₄ based photocatalysts for NO_x removal: A review. *Appl Surf Sci* 430:18–52. DOI:10.1016/j.apsusc.2017.08.192

32. Obregón S, Colón G Improved H₂ production of Pt-TiO₂/g-C₃N₄-MnO_x composites by an efficient handling of photogenerated charge pairs. *Appl Catal B-Environ* 144 (2014), 775–782. DOI:10.1016/j.apcatb.2013.07.034
33. Qian J, Yan J, Shen C, Xi F, Dong X, Liu J (2018) Graphene quantum dots-assisted exfoliation of graphitic carbon nitride to prepare metal-free zero-dimensional/two-dimensional composite photocatalysts. *J Mater Sci* 53:12103–12114. DOI:10.1007/s10853-018-2509-8
34. Reddy PVL, Kim K-H, Kavitha B, Kumar V, Raza N, Kalagara S (2018) Photocatalytic degradation of bisphenol A in aqueous media: A review. *J Environ Manage* 213:189–205. DOI:10.1016/j.jenvman.2018.02.059
35. Rochester JR, Bolden AL, Kwiatkowski CF (2018) Prenatal exposure to bisphenol A and hyperactivity in children: A systematic review and meta-analysis. *Environ Int* 114:343–356. DOI:10.1016/j.envint.2017.12.028
36. Silva GT, Carvalho KT, Lopes OF, Ribeiro C g-C₃N₄/Nb₂O₅ heterostructures tailored by sonochemical synthesis: Enhanced photocatalytic performance in oxidation of emerging pollutants driven by visible radiation. *Appl Catal B-Environ* 216 (2017), 70–79. DOI:10.1016/j.apcatb.2017.05.038
37. Sun B-W, Yu H-Y, Yang Y-J, Li H-J, Zhai C-Y, Qian D-J, Chen M (2017) New complete assignment of X-ray powder diffraction patterns in graphitic carbon nitride using discrete Fourier transform and direct experimental evidence. *Phys Chem Chem Phys* 19:38, 26072–26084. DOI:10.1039/C7CP05242A
38. The United Nations. Annex 9: Guidance on Hazards to the Aquatic Environment. 2017. <https://www.unece.org/fileadmin/DAM/trans/danger/publi/ghs/ghs_rev07/English/12e_annex9.pdf>. (Accessed 04 december 2020)
39. UNESCO. WWAP (UNESCO World Water Assessment Programme). The United Nations. World Water Development Report 2019: Leaving No One Behind. Paris, UNESCO (2019) <https://en.unesco.org/themes/water-security/wwap/wwdr/2019>, 2019 (Accessed 02 August 2020)
40. Wan J, Pu,; Wang R, Liu E, Du X, Bai X, Fan J, Hu X (2018) A facile dissolution strategy facilitated by H₂SO₄ to fabricate a 2D metal-free g-C₃N₄/rGO heterojunction for efficient photocatalytic H₂ production. *Int J Hydrogen Energy* 43:14, 7007–7019. DOI:10.1016/j.ijhydene.2018.02.134
41. Wang Y, Cao D, Liu M, Zhao X (2017) Insights into heterogeneous catalytic activation of peroxymonosulfate by Pd/g-C₃N₄: The role of superoxide radical and singlet oxygen. *Catal Commun* 102:85–88. DOI:10.1016/j.catcom.2017.08.016
42. Wang Y, Wang Y, Yu L, Wang J, Du B, Zhang X (2019) Enhanced catalytic activity of templated-double perovskite with 3D network structure for salicylic acid degradation under microwave irradiation: Insight into the catalytic mechanism. *Chem Eng J* 368:115–128. DOI:10.1016/j.cej.2019.02.174
43. Wassenaar PNH, Trasande L, Legler J Systematic review and meta-analysis of early-life exposure to bisphenol A and obesity-related outcomes in rodents. *Environ. Health Perspect.*,125 (2017) 10, 106001-1-106001-15. DOI: 10.1289/EHP1233
44. Yiantzi E, Psillakis E, Tyrovola K, Kalogerakis N Vortex-assisted liquid–liquid microextraction of octylphenol, nonylphenol and bisphenol-A. *Talanta*, 80, (2010) 5, 2057–2062. DOI: 10.1016/j.talanta.2009.11.005
45. Zhao J, Wang X, Xu Z, Loo JSC (2014) Hybrid catalysts for photoelectrochemical reduction of carbon dioxide: A prospective review on semiconductor/metal complex co-catalyst systems. *J Mater Chem* 2 37:15228–15233. DOI:10.1039/C4TA02250E
46. Ziv-Gal A, Flaws JA (2016) Evidence for bisphenol A-induced female infertility: A review (2007–2016). *Fertil Steril* 106(4):827–856. DOI:10.1016/j.fertnstert.2016.06.027

Figures

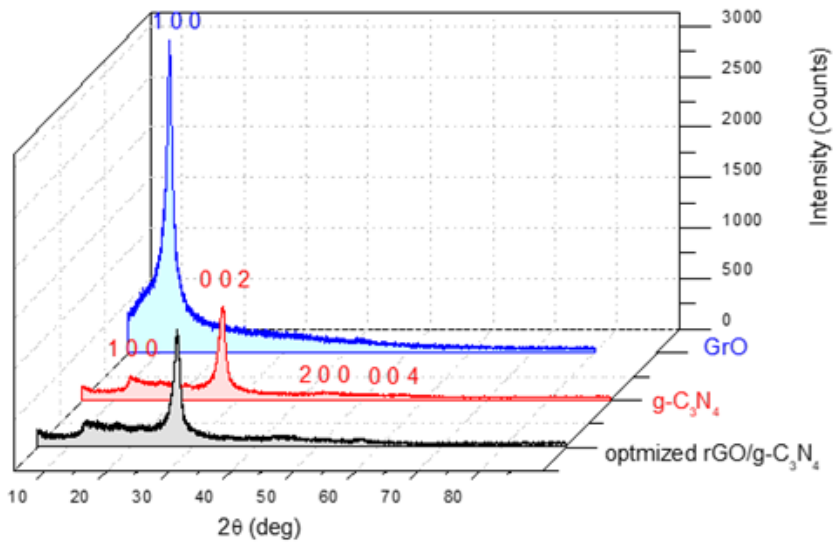


Figure 1

XRD of graphite oxide (GrO), graphitic carbon nitride (g-C₃N₄), and the composite in optimized conditions

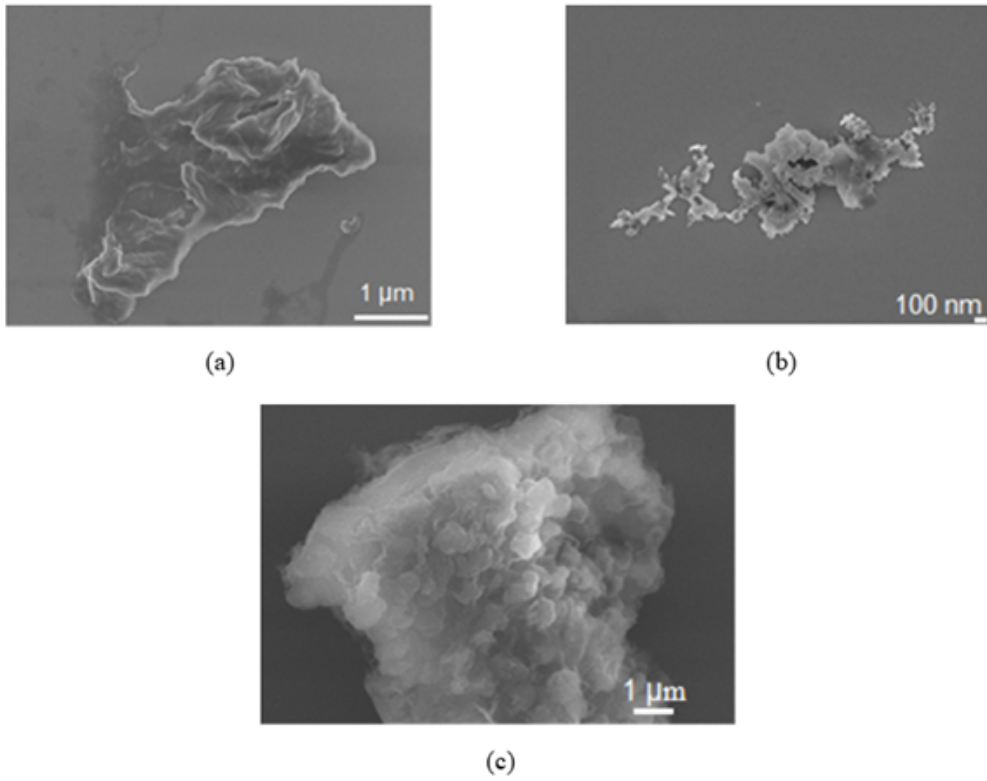


Figure 2

Scanning Electron Microscopy of (a) GrO (b) g-C₃N₄ (c) optimized rGO/g-C₃N₄

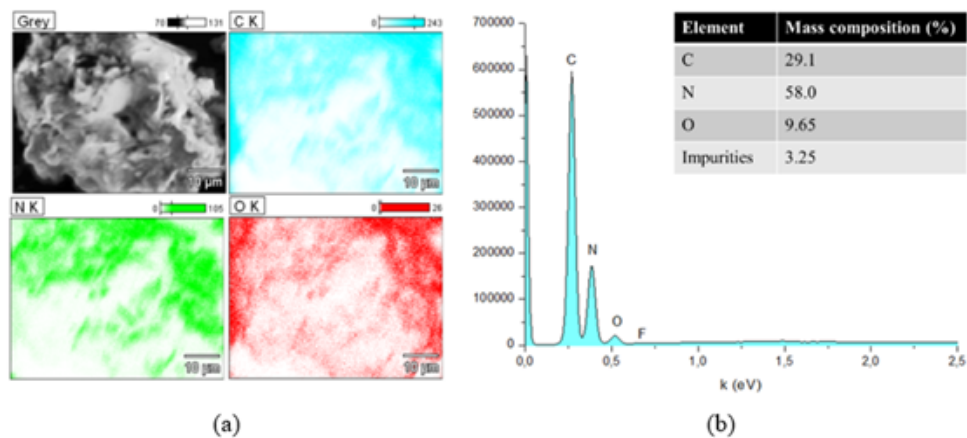


Figure 3

EDS (a) distribution and (b) spectrum for the optimized rGO/g-C₃N₄

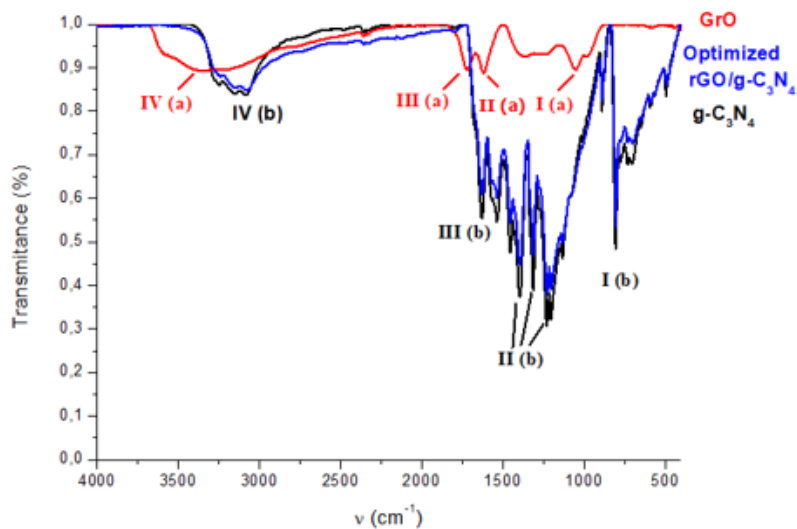


Figure 4

FTIR spectra of precursors and the optimized composite

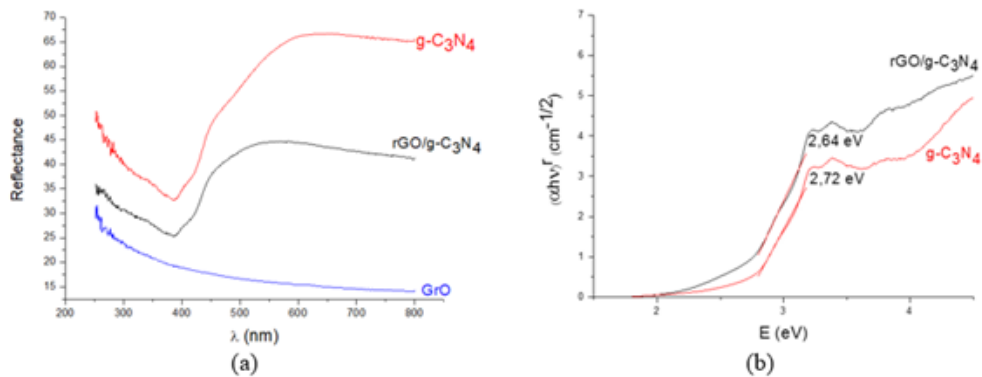


Figure 5

(a) DRS and (b) Tauc Plot of precursors and the optimized composite

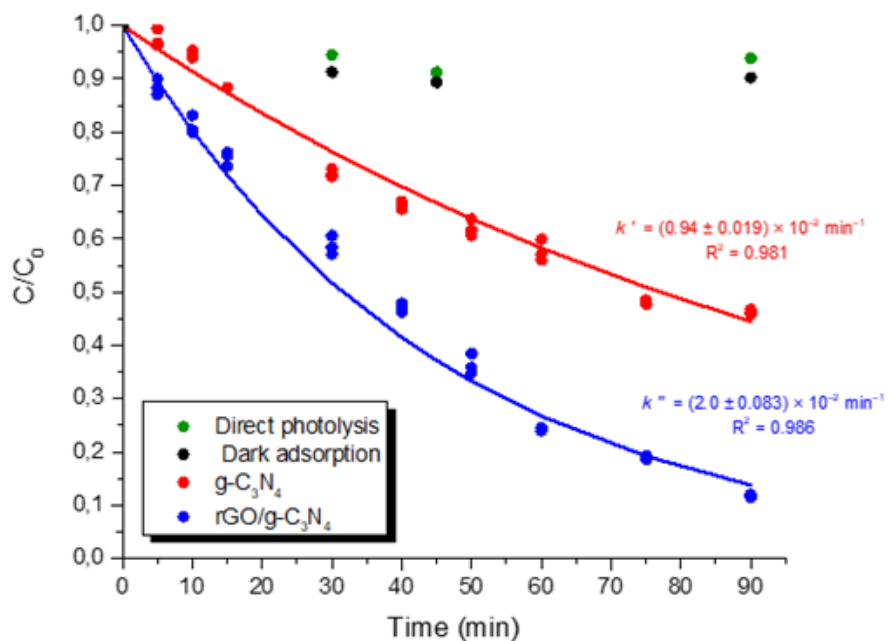


Figure 6

BPA Removal kinetics

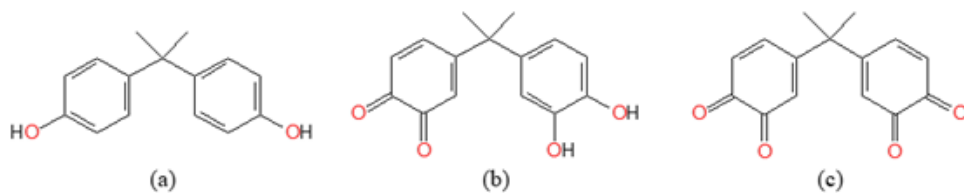


Figure 7

a) BPA structure and the proposed ones for (b) DP1 and (c) DP2

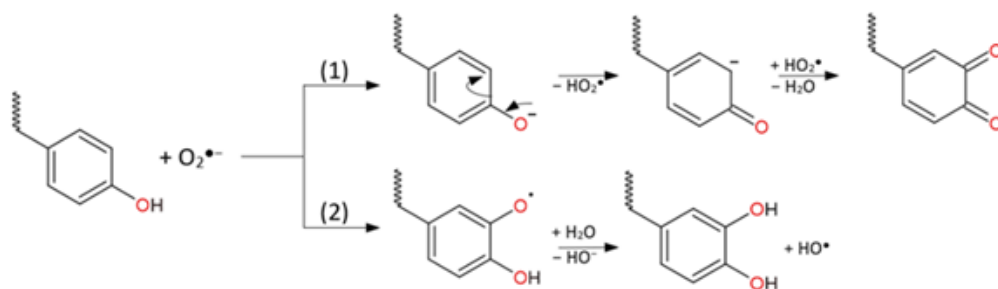


Figure 8

Proposed mechanism of oxidation of the phenolic rings of BPA

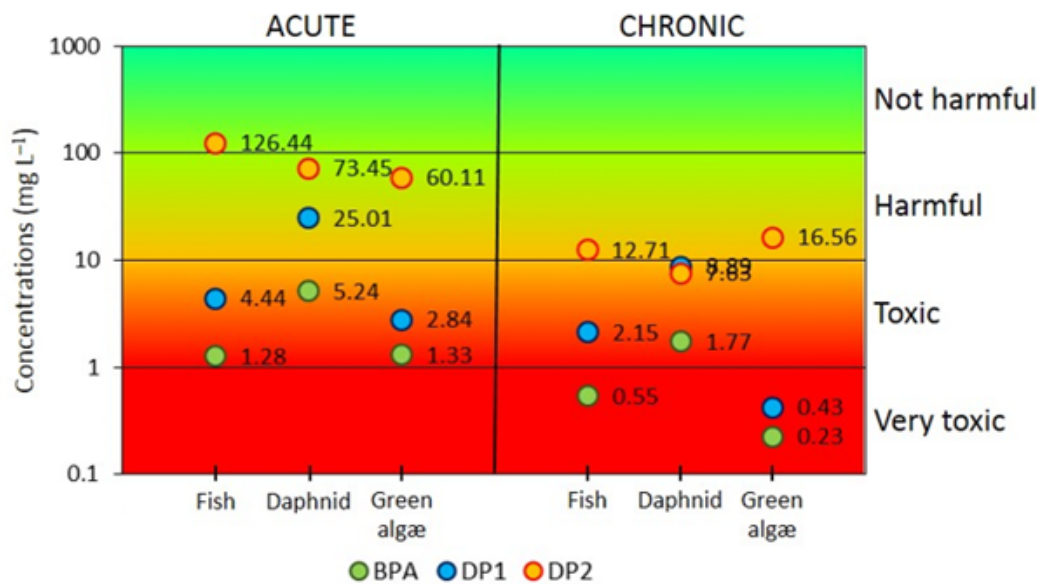


Figure 9

Estimated BPA, DP1, and DP2 acute* and chronic** ecotoxicities (ECOSAR 2.0 software)) * Fish and Daphnid (LC50), Green algæ (EC50); LC50 = Lethal Concentration to 50% of the population; EC50 = Effect Concentration to 50% of the population. ** Fish, Daphnid, and Green algæ (ChV); ChV = Chronic Value .

Supplementary Files

This is a list of supplementary files associated with this preprint. Click to download.

- [supplementarymaterialESRP.docx](#)